metals

MDPI

Article

Effect of Carbon Addition and Mechanical Activation on FeNi Alloys for Permanent Magnet Applications

Valmir R. da Silva [1], Øystein S. Fjellvåg [1], Anuj Pokle [2], Bjørn C. Hauback [1] and Stefano Deledda [1,*]

[1] Department for Hydrogen Technology, Institute for Energy Technology, 2007 Kjeller, Norway; valmir.silva@ife.no (V.R.d.S.); bjorn.hauback@ife.no (B.C.H.)
[2] Department of Physics and Centre for Materials Science and Nanotechnology, University of Oslo, 0313 Oslo, Norway; anuj.pokle@fys.uio.no
* Correspondence: stefano.deledda@ife.no

Abstract: Tetrataenite is a promising candidate for rare earth-free permanent magnets due to its low cost and intrinsic magnetic properties. This work investigates the effect of combined milling at liquid nitrogen temperatures (cryomilling) and the addition of carbon as an interstitial element for promoting the formation of tetrataenite. Crystal structure, microstructure, and magnetic properties are investigated to understand the influence of mechanical processing and compositional modifications. No unambiguous evidence of the ordered phase of tetrataenite is found in the structural characterization. However, using Scanning Transmission Electron Microscopy (STEM) and powder X-ray diffraction (PXD) analyses, the occurrence of both twinning and stacking faults resulting from the high-energy milling process is observed, which is a relevant factor for identifying tetrataenite in FeNi alloys. The probability of a stacking fault and twinning occurring for a carbon-free FeNi sample before annealing is found to be 2% and 1.4%, respectively. After annealing, the stacking fault probability decreased to 1.2%, while that of twinning was 1.4%. By increasing the carbon concentration to 5 at.%, the stacking faults and twinning probabilities decrease slightly to 1.2% and 1.3%, respectively. The occurrence of stacking faults combined with small crystallite sizes was a hindering factor in identifying the presence of tetrataenite.

Keywords: cryomilling; rare earth-free permanent magnets; stacking faults; tetrataenite; magnetism

Citation: da Silva, V.R.; Fjellvåg, Ø.S.; Pokle, A.; Hauback, B.C.; Deledda, S. Effect of Carbon Addition and Mechanical Activation on FeNi Alloys for Permanent Magnet Applications. *Metals* **2024**, *14*, 1125. https://doi.org/10.3390/met14101125

Academic Editor: Jiro Kitagawa

Received: 30 August 2024
Revised: 27 September 2024
Accepted: 28 September 2024
Published: 2 October 2024

1. Introduction

Permanent magnets are essential and strategic components in many modern technologies [1]. They have gained a critical role in energy applications as they allow conversion between mechanical work and electricity. Therefore, their development is crucial for transitioning to renewable energy sources and adopting zero-emission technologies [2]. Consequently, the demand for permanent magnets is rapidly increasing.

Currently, several materials are being considered and investigated as so-called "gap" magnets, permanent magnets with competitive properties and costs that fill the current gap between ferrite and rare-earth-based permanent magnets [3]. Among them, the ordered tetragonal FeNi phase known as tetrataenite is regarded as one of the most promising candidates due to its intrinsic properties such as high magnetocrystalline anisotropy ($K_1 = 1.3 \times 10^6$ J.m^{-3}) and large saturation magnetization ($M_S = 1300$ kA.m^{-1}) [4]. Furthermore, the low criticality and low cost of Fe and Ni are advantages for producing permanent magnets on a large scale. On the other hand, since the discovery of the ordered phase by Néel in the 1960s [4], the production of bulk single-phase tetrataenite magnets has yet to be achieved.

Tetrataenite is a phase-centered tetragonal phase (space group P4/mmm) with a c/a ratio of ~1 and is thermodynamically stable at room temperature. However, obtaining the fully ordered tetragonal $L1_0$ tetrataenite is challenging due to the relatively low transition temperature (around 593 K) from the disordered taenite phase-centered cubic A1

phase (space group $Fm\bar{3}m$) to the ordered phase. At this temperature, the atomic diffusion is extremely slow, with an estimated one atomic jump per ten thousand years [5]. To overcome the slow diffusion, non-equilibrium processing routes have been explored, including mechanical alloying at ambient temperatures and at liquid nitrogen temperature (cryomilling) [6,7], and high-pressure torsion [8,9]. Melt-spun alloys annealed at low temperatures have also been proven to partially form the $L1_0$ phase [10]. However, to this date, the most efficient approach to achieve long-range ordering is by nitrogen insertion and topotactic extraction (NITE) developed by Goto et al. [11].

Substituting Fe or Ni in the crystalline lattice with other alloying elements has also been investigated for promoting the formation of tetrataenite, as this may affect the enthalpy of formation of tetrataenite and improve the thermodynamic driving force of the ordering process [9,12]. Recent studies have evaluated the influence of Co and Cu [13], Mo [12], and Si [14] additions on the enthalpy of formation of tetrataenite. Smaller atoms, such as P and C, that can occupy interstitial sites in the crystal structure resulting in an increase of the ordering parameter of tetrataenite were also investigated [15]. The effect of elemental additions, such as B, N, Pd, Al, Ti, Cr, and Co, on the intrinsic properties of tetrataenite, has also been investigated by first principle studies [16–19]. These studies show that it is possible to increase the enthalpy of formation and enhance the magnetic properties of the $L1_0$ phase through changes in the magnetocrystalline anisotropy and saturation magnetization.

Here, we report on the synthesis of FeNi alloys containing small carbon additions using mechanochemical methods. The aim is to explore how the crystal structure, microstructure, and magnetic properties of the material are affected by the addition of interstitial carbon and cryomilling. The overall goal is to evaluate if this is a viable strategy for promoting the formation of tetrataenite.

2. Materials and Methods

Alloys with composition $(FeNi)_{100-x}C_x$ (x = 0, 2.5 and 5 at.%) were produced by mechanical alloying of elemental powder mixtures of iron, nickel (both from Goodfellow, Cambridge, UK, >99.5% purity), and carbon black (Alfa Aesar, Haverhill, MA, USA, >99.9% purity). Mechanical alloying was performed under an argon atmosphere using a Fritsch P6 planetary ball mill (Idar-Oberstein, Germany). The milling speed was set to 350 RPM with a ball-to-powder ratio of 20:1, and the vial and balls were made of zirconia. The resulting mechanically alloyed powders were mechanically milled at liquid nitrogen temperatures (cryomilling) using a SPEX Freezer Mill 6770 (Metuchen, NJ, USA) with a stainless-steel vial and rod operating with an oscillation frequency of 12 Hz. The cryomilled powders were then sealed in quartz tubes under vacuum and annealed for 1000 h at 583 K, which is 10 K below the order–disorder transition temperature of tetrataenite. The aim of the annealing is to promote short-range atomic diffusion and possibly ordering.

Powder X-ray diffraction (PXD) was carried out in a Bruker D2 Phaser (Rheinstetten, Germany) using a Bragg Brentano configuration in a Si flat plate and Cu-Kα radiation (λ = 1.5406 Å). Synchrotron radiation powder X-ray diffraction (SR-PXD) was performed at the Swiss–Norwegian beamline (SNBL; BM01) at the European Synchrotron Radiation Facility (ESRF) in Grenoble, France, with a wavelength of λ = 0.720638 Å. The samples for the SNBL experiments were packed in 0.3 mm quartz capillaries and rotated 360 degrees during the experiments. The Rietveld method was used to refine structural and microstructural properties from the experimental powder diffraction data using Topas-Academic v.6 [20]. The occurrence of coherent planar defects was further analyzed with the software Faults v.10-2018 [21], based on DIFFAX [22].

Scanning electron microscopy (SEM) was carried out with a Hitachi SU8230 (Tokyo, Japan) ultra-high resolution cold-field emission scanning electron microscope. The samples were fixed in a conductive double-sided carbon tape without the use of any coating for characterization. High-angle annular dark field (HAADF) and bright field (BF) Scanning Transmission Electron Microscopy (STEM) images were recorded on a Thermo Fisher Scientific (Waltham, MA, USA) Cs-corrected Titan G2 60–300 kV microscope operated at 300 kV. Dark field images and selected area electron diffraction (SAED) data were acquired to identify

possible superlattice diffraction signals of the tetrataenite phase. Energy dispersive x-ray spectroscopy (EDX) maps were acquired using a Super-X EDS detector (Thermo Fisher Scientific, Waltham, MA, USA). The samples were prepared using a Helios G4 UX dual-beam FIB-SEM from Thermo Fisher Scientific (Waltham, MA, USA). STEM characterizations were realized in the Norwegian Centre for Transmission Electron Microscopy (NORTEM).

Magnetization curves were measured with a vibrating sample magnetometer (VSM) from Lake Shore located at the Nanostructures and Functional Materials (NAFUMA) group at the University of Oslo. A full loop measurement was performed using an 11.2 kOe maximum field with a 14 Oe step at room temperature.

3. Results

Mechanically alloyed single-phase fcc FeNi was obtained after 5 h of ball milling of the elements. SEM shows that the particle size of the powder is between 5 and 100 µm (Figure 1). This large size distribution is expected due to the characteristics of the milling process [23]. In contrast, 3 h of cryomilling resulted in a more uniform size distribution, ranging from 5 to 70 µm, and the morphology of the particles was more spherical. Annealing imposed no significant morphological changes. On average, the powder without carbon showed particles ranging from 4 to 50 µm. The samples with added carbon showed larger particles ranging from 5 to 100 µm, as shown in Supporting Information (SI), Figure S1. This suggests the possibility that carbon also contributes as a process control agent during milling. No significant difference was observed between the samples with 2.5 and 5.0 at.% carbon.

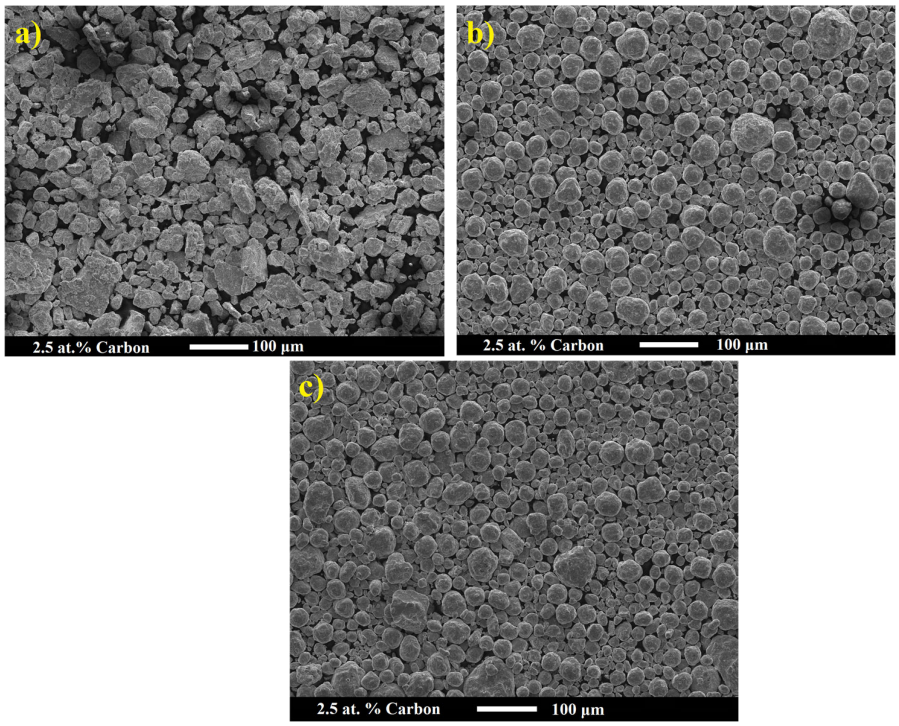

Figure 1. SEM images of powder containing 2.5 at.% of C after (**a**) ball milling, (**b**) cryomilling (180 min), and (**c**) subsequent annealing.

The microstructures and defects of the annealed samples containing 2.5 and 5 at.% carbon were further evaluated by STEM and High-Resolution TEM (HRTEM) (see Figure 2a,b, respectively). We estimate the crystallite sizes by STEM and TEM techniques to be between 5 nm and 60 nm. In addition, a notable presence of planar defects distributed throughout the sample was observed (see arrows in Figure 2). HRTEM images shown in Figure 2 suggest a higher density of defects associated with the increased carbon concentrations.

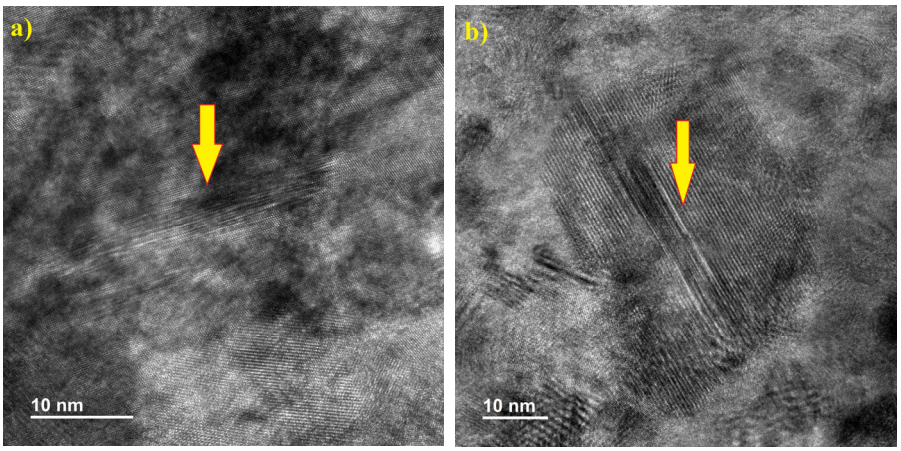

Figure 2. HRTEM images of annealed samples with (**a**) 2.5 at.% of carbon and (**b**) 5 at.% of carbon. The arrows indicate planar defects.

STEM images and the corresponding EDX mapping presented in Figure 3 indicate the elemental distribution of iron (f), nickel (g), and carbon (h). The results show a homogenous distribution of carbon, suggesting the incorporation of carbon in the FeNi crystal structure. This is further corroborated by the PXD data (see Figure 4), showing that no significative quantities of secondary phases are present, except ZrO_2 stemming from the balls and vials during the ball milling process. EDX analysis also indicates that both iron and nickel are homogenously distributed, although small heterogeneities are observed, some grains being richer in either iron or nickel, as shown in Figure S2. We also performed SAED to search for reflections from the ordered $L1_0$ phase at a microscopic level (see Figure S3). No such superlattice reflections were observed in the SEAD, indicating the presence of the disordered phase only.

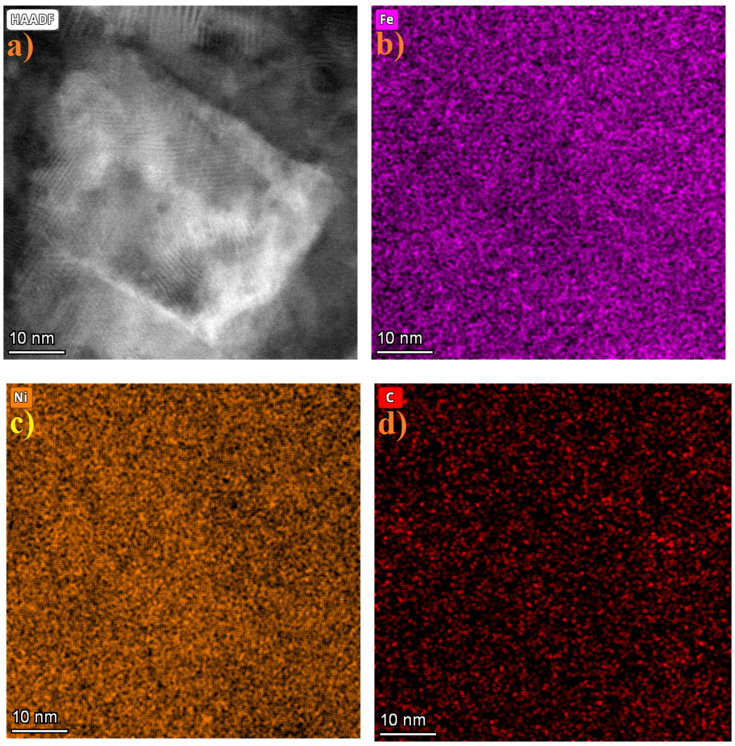

Figure 3. STEM images of the sample with 2.5 at.% C after annealing. HAADF (**a**) and EDS EDX mapping of Fe, Ni, C, (**b**–**d**), respectively.

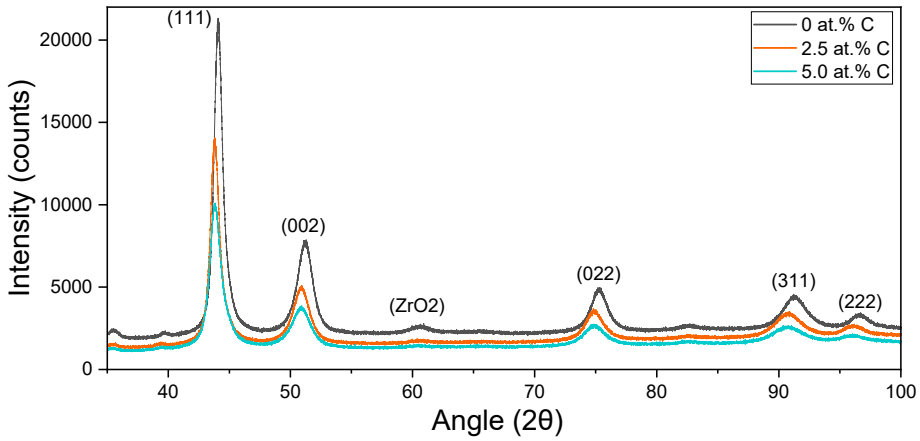

Figure 4. PXD data (Cu-Kα radiation) of ball-milled samples without carbon (black), 2.5 at.% of carbon (orange), and 5.0 at.% (cyan).

Figure 4 shows PXD data for the ball-milled samples with different carbon concentrations. The main phase is consistent with a disordered fcc FeNi solid solution. The Bragg peaks become broader with increasing carbon concentration. This indicates a change in particle size or strain as a function of carbon addition. In addition, there is a slight shift towards lower Bragg angles with increasing carbon concentration, indicating an increased unit cell volume for higher nominal carbon contents. Bragg peaks characteristic for ZrO_2 were also observed in PXD data; the contamination source is the vial and the balls used in the ball milling process.

The microstructure of the FeNi powder samples after each processing step was evaluated by PXD (see Figure 5). The diffraction pattern for the ball-milled alloyed $(FeNi)_{97.5}C_{2.5}$ sample (blue curve) shows relatively broad peaks, likely due to the small crystallite size. After cryomilling (black curve), the Bragg peaks are slightly broader and shifted towards lower scattering angles. This indicates a possible further reduction of the crystallite size and an increase in the strain. No additional diffraction peaks except the already mentioned ZrO_2 were observed. The PXD pattern for the sample after annealing (red curve) almost overlaps that of the ball-milled sample, which suggests possible crystallite growth and strain reduction during annealing.

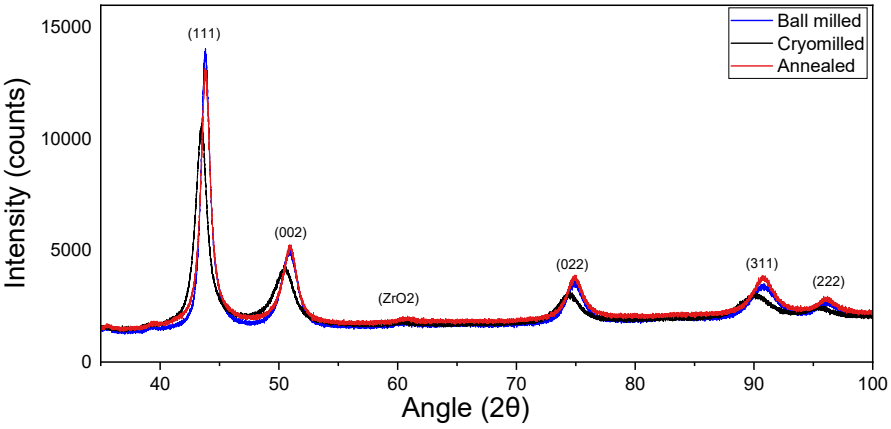

Figure 5. PXD data (Cu-Kα radiation) of samples containing 2.5 at.% of carbon after ball milling (blue), cryomilling (black), and annealing (red).

Cryomilled and annealed samples were also characterized with synchrotron PXD at BM01 SNBL (ESRF). The samples were phase-pure without any secondary phases, no superlattice peaks, or the split of Bragg peaks at higher angles, characteristic of the ordered $L1_0$ FeNi in the diffraction patterns (see SI: Figure S4).

As a first step, a standard Rietveld refinement was performed on synchrotron data using Topas-Academic. However, the obtained fit showed significant discrepancies, in particular for the (111) and (222) Bragg peaks, as shown in Figure S4. These discrepancies suggest the presence of structural defects within the samples, such as stacking faults and twins. In the literature, the heightened intensity of the (111) peak may also be attributed to twinning, while the relative displacement between the (111) and (200) peaks is indicative of stacking faults [24,25]. These defects are typically generated during high-energy milling processes [26], and the chosen heat treatment temperature appears insufficient to promote recrystallization and anneal them out.

To account for the occurrence of stacking faults and twinning possibly present in the material, the software Faults was used to perform further refinements. A model of fcc iron and nickel randomly distributed was used, and the probability of a fault occurring in the (111) direction was calculated. The probability of both an intrinsic stacking fault and the probability of a twin occurring were considered. Table 1 shows the description of the faults compared to the regular ABC stacking for a cubic system.

Table 1. Difference in the sequence of the lattice plane for a regular fcc stacking with stacking fault and twin.

Defect	Sequence of Lattice Plane
Regular fcc stacking	ABCABCAB
Intrinsic S.F.	ABCAB | ABC
Twin	ABC | B | A | C | . . .

Initial evaluations of a model with stacking faults and no twin faults show that the quality of the Rietveld refinements improves significantly. The Rwp illustrates this improvement for an annealed sample containing 5 at.% of carbon, which improves from 6.56 to 3.50% when a 2.0% probability of stacking faults occurrence is included.

By refining the stacking fault probability at different constant probabilities of twin faults, the refinements continued to improve. The Rwp decreased slightly from 3.50 to 3.37% when the probability of twin faults was changed from 0 to 1.3%. This finding agrees with our observations in STEM, with stacking and twin faults in the sample. Our final model for this sample has 1.5% stacking faults and 2.3% twin faults, and the Rietveld refinements are shown in Figure 6. A considerably better model was obtained when accounting for stacking faults and twins compared to the previous models. We found the approach of combining stacking faults and twin faults to yield improved fits for all samples, and we thus expanded this approach to all samples. The results of the refinements are summarized in Table 2.

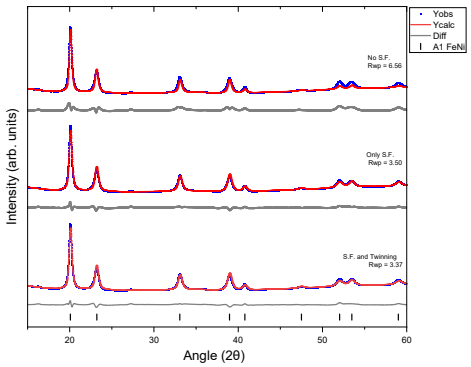

Figure 6. Rietveld refinements of synchrotron X-ray data (λ = 0.720638 Å) for carbon-free sample cryomilled for 180 min and annealed. Top: cubic phase without defects, middle: stacking faults considered, bottom: stacking faults and twinning. The final model suggests a probability of 1.5% of stacking fault occurrence and a 2.3% probability of twinning. The model was calculated using Faults.

Table 2. Refinement results for cryomilled samples before and after annealing using Faults software: lattice parameter (a), calculated stacking faults probability (S.F.) and twin probability (Twin), total faults, and weighted profile R-factor (Rwp) are presented. PXD data were acquired at the BM-01 in ESRF (λ = 0.720638 Å).

Composition	Cryomill Time (min)	a (Å)	S.F. (%)	Twin (%)	Total Faults (%)	Rwp (%)
Carbon-free	30	3.58(1)	2.0	1.4	3.4	5.77
	30 *	3.58(1)	1.2	1.4	2.6	5.73
	60	3.59(1)	2.2	1.8	4.0	4.10
	60 *	3.58(1)	5.2	1.7	6.9	4.83
	120	3.58(1)	2.6	2.3	4.9	4.20
	120 *	3.58(1)	4.1	2.1	6.2	6.12
	180	3.59(1)	3.0	2.5	5.5	3.46
	180 *	3.59(1)	1.5	2.5	4.0	3.37
2.5 at.%	30	3.59(1)	1.0	1.5	2.5	5.13
	30 *	3.59(1)	0.7	1.3	2.0	3.92
	60	3.60(1)	3.1	1.5	4.6	4.53
	60 *	3.59(1)	0.8	1.7	2.5	3.57
	120	3.60(1)	2.2	2.3	4.5	4.33
	120 *	3.59(1)	2.6	2.2	4.8	5.10
	180	3.60(1)	2.8	2.5	5.3	3.26
	180 *	3.59(1)	2.6	2.2	4.8	3.75
5.0 at.%	30 **	3.60(1)	2.7	1.5	4.2	9.05
	30 *	3.58(1)	1.2	1.3	2.5	3.82
	60	3.60(1)	3.7	1.9	5.6	4.25
	60 *	3.58(1)	1.7	1.6	3.3	3.82
	120	3.60(1)	0.7	2.1	2.8	5.15
	120 *	3.59(1)	0.1	2.0	2.1	5.40
	180	3.61(1)	4.7	2.5	7.2	3.75
	180 *	3.59(1)	1.9	2.2	4.1	3.40

* After annealing. ** PXD data obtained using Cu-Kα radiation (λ = 1.5406 Å).

The model used in Faults indicates that the probability of stacking faults, in general, was reduced after annealing. For example, a carbon-free sample cryomilled for 30 min has a probability of stacking faults of 3% before and 1.5% after annealing. Nevertheless, the calculated twin probability showed only a small reduction after heat treatment. The results indicate that heat treatment, in general, promotes the reduction of total planar faults in the material (staking faults + twins). However, the temperature was constrained due to the low disorder–order temperature of $L1_0$, and the complete elimination of such defects was not possible. Carbon concentration had no significant contribution to the number of faults present in the samples.

Magnetic hysteresis loops were measured for all samples at room temperature to evaluate the saturation magnetization. Figure 7 shows the magnetization curves for the carbon-free (black), 2.5 at.% (blue), and 5.0 at.% (red) of carbon samples after cryomilling and subsequent annealing. The curves show a soft magnetic behavior for all compositions with only a small difference in M_S values. The M_S value for the carbon-free sample was 110 emu/g, while for the samples with 2.5 at.% and 5.0 at.% of carbon, M_S values were 128 and 115 emu/g, respectively. No further modification of the coercivity is detected through the processing. Had the ordered $L1_0$ phase been present in any of the samples, signs of magnetic hardening would have been observed. This supports our interpretation of the diffraction data; the samples consist of the disordered A1 structure, and microstructural refinement through cryomilling and subsequent annealing does not promote the formation of the $L1_0$ phase.

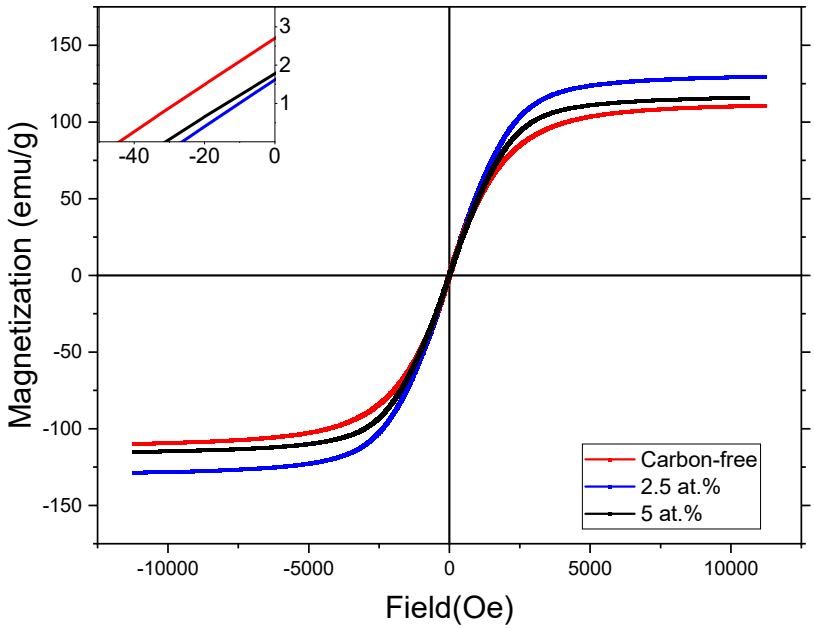

Figure 7. Magnetization curves for samples cryomilled for 180 min and annealed. Carbon-free sample (red), and with 2.5 at.% of carbon (blue) and 5 at.% of carbon (black).

The incorporation of carbon alongside the employed mechanical activation techniques did not appear to induce the formation of the $L1_0$ phase or any substantial ordering processes. Analysis of STEM images demonstrated that the adopted milling procedures effectively promoted the development of a single-phase cubic FeNi structure with small crystallite sizes. This finding was corroborated by PXD analysis. Rietveld refinements incorporating stacking faults and twinning for a face-centered cubic equiatomic FeNi phase yielded a satisfactory fit to the diffraction data, suggesting that the observed shifts in Bragg peaks originated from the presence of planar defects. Magnetic characterization of the samples revealed no significant enhancement in coercivity.

4. Discussion

In this work, we investigated the influence of cryomilling and subsequent annealing in FeNi powders containing different carbon concentrations on the possible formation of tetrataenite. The decision to use carbon as an interstitial element was inspired by previous studies on Mn-Al-C systems, where carbon was shown to promote the formation and stability of the tetragonal τ-phase [27,28]. Interstitial elements such as carbon, nitrogen, and boron might also promote the uniaxial magnetic anisotropy and modify the enthalpy of formation of the ordered $L1_0$ phase as proposed by ab initio studies seen in [16].

The alloys were produced via a high-energy planetary ball mill and subsequently cryomilled. After the cryomill process, a heat treatment was performed at 583 K for 1000 h under vacuum. The aim of the annealing step is to promote short-range atomic diffusion and, in turn, the formation of tetrataenite. The latter is the most stable phase at this temperature. Higher annealing temperatures can enhance atomic diffusion, in principle decreasing the time needed for the formation of tetrataenite. However, the order–disorder transition for tetrataenite is estimated to be around 593 K [5], meaning that above this temperature, tetrataenite is no longer the most stable phase. Hence, the annealing temperature of 583 K chosen in this work, 10 K below the order–disorder transition temperature, should ensure maximum atomic short-range diffusion while remaining in the stability range for the $L1_0$ tetrataenite phase. Having fixed the annealing temperature, time was left as the primary variable for annealing and was selected based on similar studies aimed at the production of tetrataenite in a feasible laboratory timescale.

The results obtained via PXD and SEM on the ball-milled powders indicated that the process was sufficient to promote the conversion of α-Fe and pure nickel to an fcc FeNi phase. Rietveld refinements of cryomilled powders, initially considering a single-disordered A1 phase, demonstrate a consistent increase in lattice parameters as a function of nominal carbon content and a concurrent decrease in crystallite size with extended milling durations. However, the small additions of carbon to the alloy did not promote the formation of the ordered tetragonal tetrataenite phase at the annealing conditions used in this work. This is in contrast to what is observed in the Mn-Al-C system, where the tetragonal τ-phase is stabilized by small additions of C. The different outcome may be ascribed to the inherently different structural and thermodynamic characteristics between the fully ordered tetragonal tetrataenite and the partially ordered metastable τ-MnAl phase. For the latter, the main effect of carbon is to increase its stability against decomposition into thermodynamically stable phases. On the other hand, the challenge for tetrataenite is its formation and not so much its stability. In this respect, carbon additions in the FeNi system were not effective for improving thermodynamics or kinetics, e.g., atomic diffusion, towards the formation of ordered tetrataenite.

TEM images show planar defects in the samples, which also indicates that the crystallite sizes varied between 5 nm and 60 nm. Notably, the presence of planar defects, including stacking faults and twinning, is observed, indicating that such microstructural features should be considered when evaluating structural data.

The precise identification and quantification of the $L1_0$ phase dispersed within the material remains a challenging endeavor. This difficulty arises from the similar X-ray scattering factors of Fe and Ni, leading to subtle variations in the superstructure Bragg peaks observed in PXD analysis. Furthermore, the combination of small crystallite size with prevalent stacking faults and twinning phenomena contributes to significant peak broadening, further complicating characterization. Consequently, quantifying the ordered phase within FeNi alloys necessitates the application of complementary characterization techniques, as demonstrated by Peña Rodrigues et al. [7].

With our analyses using Faults, we take microstructural aspects into account when calculating the stacking fault probabilities after the mechanical activation processes of cryomilling and subsequent annealing. By increasing the carbon concentration, an increase in the probability of stacking faults and twinning was observed.

The peak broadening from stacking and twin faults significantly impacts the diffraction patterns, broadening specific peaks and changing the peak intensity. The quality of our refinements with stacking and faults shows that microstructural factors cannot be disregarded when analyzing FeNi alloys. These features can easily be confused with broadening from phase co-existence, which we have described with a purely microstructural model, which we believe is a more likely approach. We, therefore, encourage the evaluation using a microstructural model for FeNi and similar systems.

Stacking faults and twinning occur due to high-energy ball milling and cryogenic milling. An annealing temperature higher than the one used in this study must be used to eliminate such defects. However, this is not possible due to the restrictions imposed by the tetrataenite's low order–disorder temperature. The effect of stacking faults and twinning on the formation of the $L1_0$ phase is not clearly understood, but it is worth noting that Wang et al. reported the presence of stacking faults on FeNi alloys, which was suggested to accelerate the formation of tetrataenite [29]. At the same time, nanotwinned regions were observed in FeNi alloys containing tetrataenite from cosmic matter [30]. Nanotwinned regions can also promote the formation of the intermediary FeNiN phase during the NITE processing to transform the A1 to $L1_0$ phase [31]. Hence, a high density of defects is expected to arise from the tetrataenite-forming processes, and they must, therefore, be carefully taken into account during the structural characterization of the A1 and $L1_0$ phases.

The magnetic properties measured using VSM show a soft magnetic behavior with low coercivity values for annealed samples with different carbon concentrations, indicating an absence of the ordered tetrataenite phase. Since no significant magnetic hardening

has been observed, it was not possible to evaluate the effect of carbon addition on the post-processed samples. Stacking faults and twins showed no direct influence on the coercivity values for the alloys. The coercivity values obtained in this study (between 60 and 20 Oe) were comparable to single-phase fcc FeNi alloys produced by ball milling reported by Guittoum et al. (between 5 and 37 Oe), where the magneto-elastic effect was the predominant factor for coercivity values [32]. When tetrataenite was present in the samples, an increase in the coercivity is expected due to the anisotropy present, i.e., as observed in the NWA 6259 meteorite (1200 Oe, measured at 5 K) [33] and ~750 Oe for melt-spun annealed samples containing Si, B, P, and Cu [10].

Bulk magnetic measurement techniques proved challenging in identifying the occurrence of an ordered phase in small quantities. No indications of the desirable magnetic properties of the tetrataenite phase were observed, supporting our microstructural model.

5. Conclusions

The use of high-energy ball milling and cryomilling has proven to be an effective method for synthesizing single-phase FeNi alloys characterized by small crystallite sizes and a high density of defects. This approach also facilitates the incorporation of interstitial light elements, which can enhance both the material properties and the kinetics of ordered phase formation. However, varying concentrations of carbon did not significantly contribute to the ordering of FeNi alloys into the tetrataenite phase, nor did they induce notable magnetic hardening.

The high defect density introduced by these processes, while theoretically enhancing atomic mobility, was insufficient to promote atomic ordering during subsequent annealing. The occurrence of stacking faults and twinning increased proportionally with cryomilling duration. Annealing the samples slightly below the order–disorder transition temperature for 1000 h generally decreased the number of planar defects, though complete elimination was not achieved.

Despite these challenges, the combined use of mechanical activation techniques and the introduction of interstitial elements remains a promising strategy for the development of rare-earth-free permanent magnets. In this respect, alternative processing techniques, such as cold rolling, can promote distinct defect features that might improve atomic mobility, and reports in the literature point in that direction [6]. Another alternative approach to tackle the challenges of tetrataenite formation is extending the annealing times. However, extremely long annealing times are impractical for research and industrial purposes. Finally, based on first-principles calculations and experimental studies reported in the literature, it is worth further investigating FeNi alloys containing small additions of interstitial elements like B, P, and N, which have the potential to promote the formation of ordered tetrataenite by increasing atomic mobility and ordering processes. This can be crucial for enabling the introduction of tetrataenite in permanent magnet applications.

Supplementary Materials: The following supporting information can be downloaded at: https://www.mdpi.com/article/10.3390/met14101125/s1. Figure S1: SEM images of 5-h ball-milled powders, carbon-free (a), and 2.5 at.% of carbon (b). Particle size ranges from 5 to 100 μm; Figure S2: STEM images of annealed samples with 5 at.% of carbon. (a) Bright field, (b) dark field, (c) HAADF and EDS mapping of Fe, Ni, C, (d), (e), and (f) respectively. Region deliberately selected to show small heterogeneity between elements; Figure S3: STEM image of a cryomilled and subsequently annealed sample with 5 at.% of carbon (a), and SAED from the circled area (b). Since the selected area is larger than the crystallite size, it results in a polycrystalline diffraction pattern. Hence, it remains to be clarified if carbon and its relative content affect local ordering and result in the formation of the $L1_0$ phase; Figure S4: Rietveld refinement of synchrotron PXD data for the carbon-free sample, cryomilled after 3 h, and annealed for 1000 h at 583 K. Blue dots represent the measured data, the red line is the single-phase model used in the refinement, and the gray line is the difference. Rwp: 2.80.

Author Contributions: Conceptualization, V.R.d.S., S.D. and B.C.H.; methodology, V.R.d.S. and S.D.; validation, V.R.d.S., S.D., Ø.S.F. and B.C.H.; formal analysis, S.D. and B.C.H.; investigation, V.R.d.S., Ø.S.F. and A.P.; resources, S.D.; data curation, V.R.d.S., S.D., A.P. and B.C.H.; writing—original draft preparation, V.R.d.S.; writing—review and editing, V.R.d.S., Ø.S.F., A.P. and S.D.; visualization, V.R.d.S., Ø.S.F., B.C.H. and S.D.; supervision, S.D.; project administration, S.D.; funding acquisition, S.D. All authors have read and agreed to the published version of the manuscript.

Funding: This research was funded by the Research Council of Norway (NFR, project no. 303563—REFINE).

Data Availability Statement: The raw data supporting the conclusions of this article will be made available by the authors on request.

Acknowledgments: Ø.S.F. acknowledges funding from NFR through project no. 325345. The skillful assistance of the staff at the Swiss Norwegian Beam Line, ESRF (Synchrotron PXD), NORTEM Center (TEM), and the Nanostructures and Functional Materials (NAFUMA) group (University of Oslo) (VSM) are also greatly acknowledged.

Conflicts of Interest: The authors declare no conflict of interest.

References

1. Coey, J.M.D. Permanent Magnet Applications. *J. Magn. Magn. Mater.* **2002**, *248*, 441–456. [CrossRef]
2. Gutfleisch, O.; Willard, M.A.; Brück, E.; Chen, C.H.; Sankar, S.G.; Liu, J.P. Magnetic Materials and Devices for the 21st Century: Stronger, Lighter, and More Energy Efficient. *Adv. Mater.* **2011**, *23*, 821–842. [CrossRef] [PubMed]
3. Coey, J.M.D. Permanent Magnets: Plugging the Gap. *Scr. Mater.* **2012**, *67*, 524–529. [CrossRef]
4. Néel, L.; Pauleve, J.; Pauthenet, R.; Laugier, J.; Dautreppe, D. Magnetic Properties of an Iron—Nickel Single Crystal Ordered by Neutron Bombardment. *J. Appl. Phys.* **1964**, *35*, 873–876. [CrossRef]
5. Bordeaux, N.; Montes-Arango, A.M.; Liu, J.; Barmak, K.; Lewis, L.H. Thermodynamic and Kinetic Parameters of the Chemical Order-Disorder Transformation in L10 FeNi (Tetrataenite). *Acta Mater.* **2016**, *103*, 608–615. [CrossRef]
6. Montes-Arango, A.M.; Marshall, L.G.; Fortes, A.D.; Bordeaux, N.C.; Langridge, S.; Barmak, K.; Lewis, L.H. Discovery of Process-Induced Tetragonality in Equiatomic Ferromagnetic FeNi. *Acta Mater.* **2016**, *116*, 263–269. [CrossRef]
7. Rodríguez, V.A.P.; Rojas-Ayala, C.; Medina, J.M.; Cabrera, P.P.; Quispe-Marcatoma, J.; Landauro, C.V.; Tapia, J.R.; Baggio-Saitovitch, E.M.; Passamani, E.C. $Fe_{50}Ni_{50}$ Synthesized by High Energy Ball Milling: A Systematic Study Using X-ray Diffraction, EXAFS and Mössbauer Methods. *Mater. Charact.* **2019**, *149*, 249–254. [CrossRef]
8. Lee, S.; Edalati, K.; Iwaoka, H.; Horita, Z.; Ohtsuki, T.; Ohkochi, T.; Kotsugi, M.; Kojima, T.; Mizuguchi, M.; Takanashi, K. Formation of FeNi with L10-Ordered Structure Using High-Pressure Torsion. *Philos. Mag. Lett.* **2014**, *94*, 639–646. [CrossRef]
9. Ulyanov, M.; Taskaev, S.; Shevyrtalov, S.; Medvedskaya, P.; Gunderov, D. Structural Properties of $Fe_{49}Ni_{49}Ti_2$ Alloy Deformed by High Pressure Torsion. *AIP Adv.* **2021**, *11*, 025311. [CrossRef]
10. Makino, A.; Sharma, P.; Sato, K.; Takeuchi, A.; Zhang, Y.; Takenaka, K. Artificially Produced Rare-Earth Free Cosmic Magnet. *Sci. Rep.* **2015**, *5*, 16627. [CrossRef]
11. Goto, S.; Kura, H.; Watanabe, E.; Hayashi, Y.; Yanagihara, H.; Shimada, Y.; Mizuguchi, M.; Takanashi, K.; Kita, E. Synthesis of Single-Phase L10-FeNi Magnet Powder by Nitrogen Insertion and Topotactic Extraction. *Sci. Rep.* **2017**, *7*, 13216. [CrossRef] [PubMed]
12. Maât, N.; McDonald, I.; Barua, R.; Lejeune, B.; Zhang, X.; Stephen, G.M.; Fisher, A.; Heiman, D.; Soldatov, I.V.; Schäfer, R.; et al. Creating, Probing and Confirming Tetragonality in Bulk FeNi Alloys. *Acta Mater.* **2020**, *196*, 776–789. [CrossRef]
13. Kołodziej, M.; Śniadecki, Z. The Formation of Structural Disorder in FeNi-Based Alloys—Theoretical Approach. *Mater. Lett.* **2022**, *326*, 132917. [CrossRef]
14. Hao, Z.; Wei, L.; Wang, Y.; Kawazoe, Y.; Liang, X.; Umetsu, R.; Yodoshi, N.; Tong, X.; Xia, W.; Zhang, Y.; et al. Effect of Si Addition on the Magnetic Properties of FeNi-Based Alloys with L10 Phase through Annealing Amorphous Precursor. *J. Alloys Compd.* **2022**, *920*, 166029. [CrossRef]
15. Ivanov, Y.P.; Sarac, B.; Ketov, S.V.; Eckert, J.; Greer, A.L. Direct Formation of Hard-Magnetic Tetrataenite in Bulk Alloy Castings. *Adv. Sci.* **2022**, *10*, 2204315. [CrossRef] [PubMed]
16. Tuvshin, D.; Ochirkhuyag, T.; Hong, S.C.; Odkhuu, D. First-Principles Prediction of Rare-Earth Free Permanent Magnet: FeNi with Enhanced Magnetic Anisotropy and Stability through Interstitial Boron. *AIP Adv.* **2021**, *11*, 015138. [CrossRef]
17. Matar, S.F.; Houari, A.; Eyert, V. Nitrided FeNi: Chemical versus Magnetovolume Effects from Ab Initio. *J. Magn. Magn. Mater.* **2019**, *491*, 165555. [CrossRef]
18. Rani, P.; Singla, R.; Thakur, J.; Reshak, A.H.; Kashyap, M.K. Enhancement in Magnetic Parameters of L10-FeNi on Pd-Substitution for Permanent Magnets. *Indian J. Phys.* **2023**, *97*, 67–72. [CrossRef]
19. Tian, L.Y.; Gutfleisch, O.; Eriksson, O.; Vitos, L. Alloying Effect on the Order–Disorder Transformation in Tetragonal FeNi. *Sci. Rep.* **2021**, *11*, 5253. [CrossRef]
20. Coelho, A.A. TOPAS and TOPAS-Academic: An Optimization Program Integrating Computer Algebra and Crystallographic Objects Written in C++: An. *J. Appl. Crystallogr.* **2018**, *51*, 210–218. [CrossRef]

21. Casas-Cabanas, M.; Reynaud, M.; Rikarte, J.; Horbach, P.; Rodríguez-Carvajal, J. FAULTS: A Program for Refinement of Structures with Extended Defects. *J. Appl. Crystallogr.* **2016**, *49*, 2259–2269. [CrossRef]
22. Treacy, M.M.J.; Newsam, J.M.; Deem, M.W. A General Recursion Method for Calculating Diffracted Intensities from Crystals Containing Planar Faults. *Proc. R. Soc. Lond. A* **1991**, *433*, 499–520. [CrossRef]
23. Gheisari, K.; Javadpour, S.; Oh, J.T.; Ghaffari, M. The Effect of Milling Speed on the Structural Properties of Mechanically Alloyed Fe-45%Ni Powders. *J. Alloys Compd.* **2009**, *472*, 416–420. [CrossRef]
24. Martin, S.; Ullrich, C.; Imek, D.; Martin, U.; Rafaja, D. Stacking Fault Model of-Martensite and Its DIFFaX Implementation. *J. Appl. Crystallogr.* **2011**, *44*, 779–787. [CrossRef]
25. Velterop, L.; Delhez, R.; De Keijser, T.H.; Mittemeijer, E.J.; Reefman, D. X-ray Diffraction Analysis of Stacking and Twin Faults in f.c.c. Metals: A Revision and Allowance for Texture and Non-Uniform Fault Probabilities. *J. Appl. Crystallogr.* **2000**, *33*, 296–306. [CrossRef]
26. Geng, Y.; Ablekim, T.; Koten, M.A.; Weber, M.; Lynn, K.; Shield, J.E. Defect Generation and Analysis in Mechanically Alloyed Stoichiometric Fe-Ni Alloys. *J. Alloys Compd.* **2015**, *633*, 250–255. [CrossRef]
27. Fang, H.; Cedervall, J.; Hedlund, D.; Shafeie, S.; Deledda, S.; Olsson, F.; Von Fieandt, L.; Bednarcik, J.; Svedlindh, P.; Gunnarsson, K.; et al. Structural, Microstructural and Magnetic Evolution in Cryo Milled Carbon Doped MnAl. *Sci. Rep.* **2018**, *8*, 2525. [CrossRef] [PubMed]
28. Øygarden, V.; Rial, J.; Bollero, A.; Deledda, S. Phase-Pure τ-MnAlC Produced by Mechanical Alloying and a One-Step Annealing Route. *J. Alloys Compd.* **2019**, *779*, 776–783. [CrossRef]
29. Wang, X.; Wen, T.; Sun, L.; Lou, J.; He, H.; Chen, Y.; Ouyang, X. Fe-50Ni Alloy with Ordered L10 Structure Prepared by Cubic Pressing. *Mater. Lett.* **2020**, *280*, 128563. [CrossRef]
30. Langenhorst, F.; Harries, D.; Pollok, K.; Van Aken, P.A. Mineralogy and Defect Microstructure of an Olivine-Dominated Itokawa Dust Particle: Evidence for Shock Metamorphism, Collisional Fragmentation, and LL Chondrite Origin. *Earth Planets Space* **2014**, *66*, 118. [CrossRef]
31. Wang, J.; Hirayama, Y.; Liu, Z.; Suzuki, K.; Yamaguchi, W.; Park, K.; Takagi, K.; Kura, H.; Watanabe, E.; Ozaki, K. Massive Transformation in FeNi Nanopowders with Nanotwin-Assisted Nitridation. *Sci. Rep.* **2022**, *12*, 3679. [CrossRef] [PubMed]
32. Guittoum, A.; Layadi, A.; Bourzami, A.; Tafat, H.; Souami, N.; Boutarfaia, S.; Lacour, D. X-ray Diffraction, Microstructure, Mössbauer and Magnetization Studies of Nanostructured $Fe_{50}Ni_{50}$ Alloy Prepared by Mechanical Alloying. *J. Magn. Magn. Mater.* **2008**, *320*, 1385–1392. [CrossRef]
33. Lewis, L.H.; Mubarok, A.; Poirier, E.; Bordeaux, N.; Manchanda, P.; Kashyap, A.; Skomski, R.; Goldstein, J.; Pinkerton, F.E.; Mishra, R.K.; et al. Inspired by Nature: Investigating Tetrataenite for Permanent Magnet Applications. *J. Phys. Condens. Matter* **2014**, *26*, 064213. [CrossRef] [PubMed]